IEEE Access
Multidisciplinary ⋮ Rapid Review ⋮ Open Access Journal

Received 24 October 2023, accepted 20 November 2023, date of publication 24 November 2023,
date of current version 1 December 2023.

Digital Object Identifier 10.1109/ACCESS.2023.3336814

RESEARCH ARTICLE

Ray-Tracing Propagation Modeling in Urban Environment at 140 GHz for 6G Wireless Networks

NEKTARIOS MORAITIS, (Senior Member, IEEE), AND KONSTANTINA S. NIKITA, (Fellow, IEEE)
School of Electrical and Computer Engineering, National Technical University of Athens, 15773 Athens, Greece
Corresponding author: Nektarios Moraitis (morai@mobile.ntua.gr)

ABSTRACT This paper introduces a propagation study at sub-THz frequencies in an urban environment. Deterministic simulations are carried out utilizing a software tool and a high-resolution digital map of the area. Different scenarios and antenna configurations are examined, as well as the relative propagation mechanisms are described. The simulated path loss is found to be well approximated by the close-in (CI) model, delivering path loss exponents equal to 2.1, and 3.4, and shadowing factors 2.5, and 7.2 dB, for line-of-sight (LOS) and non-line-of-sight (NLOS) conditions, respectively. Links that support high data rates are feasible even at NLOS locations but for distances up to 100–150 m. The root-mean-square (rms) delay spread is found in the range of 4.8–44.2 ns and 1.7–38.3 ns, for LOS and NLOS conditions, respectively. The simulated channel exhibits frequency selective characteristics demonstrating coherence bandwidth values between 8.9 and 161.7 MHz. Finally, a multi-cluster model is found to fit well the simulated PDPs. Up to four and two clusters are observed in LOS and NLOS locations, respectively. The cluster and ray decay factors, as well as their intra- and inter-arrivals times are all found to be regulated by the propagation environment and the adopted antenna characteristics.

INDEX TERMS Channel modeling, deterministic simulations, path loss, ray-tracing, sub-THz frequencies, urban environment.

I. INTRODUCTION

There is a growing requirement for frequency spectrum, able to support an excessive number of users, very low latencies and extreme throughputs that reach Tb/s, in beyond fifth-generation (B5G) and the imminent sixth-generation (6G) wireless networks [1], [2]. Future networks envisage novel applications that extend from holographic communications and wireless cognition, up to real time sensing and precise localization [3], [4]. The current deployment of the 5G networks foresee spectrum allocations below 6 GHz (FR1), as well as in the regions of 26–28 GHz and 60 GHz (FR2). However, the usable spectrum in those bands may not entirely accomplish the bandwidth necessities of the future wireless applications [5]. To deal with those stringent spectrum constraints researchers have recently focused their interest on sub-THz frequencies, taking advantage of a wide space of spectrum that could efficiently tolerate speeds of Tb/s [6]. However, sub-THz wireless links experience, apart from extreme path loss, additional losses due to atmospheric attenuation (oxygen and water vapor, or rain in the case of outdoor environments). This entails that specific frequency segments be allocated in order to minimize the additional losses. In this context, D-band (110–170 GHz) has been proposed as an appealing solution that provides a wide bandwidth, being able to accommodate applications for the next generation networks [7].

The exploitation of the D-band for future wireless networks was initially introduced in [4], regarding indoor environments. There, path loss and materials' partition loss results were delivered based on measurements at 140 GHz, and compared with existing results at 28 and 73 GHz. On the

The associate editor coordinating the review of this manuscript and approving it for publication was Parul Garg.

other hand, there are few scientific efforts available in the existing literature where outdoor channels are studied at D-band [5], [6], [7], [8], [9], [10], [11], [12], [13]. More specifically, double directional measurements in various urban environments were carried out in [5] and [8], providing path loss results, as well as the angular and the root-mean-square (rms) delay spread characteristics of the channel (145–146 GHz). Urban microcell measurements, conducted at 142 GHz, were presented in [6], and the results were compared with similar measurements at 18, 38 and 73 GHz. The measured path loss was found to be fitted by the close-in (CI) and the multi-frequency CI (CIF) models for line-of-sight (LOS) and non-line-of-sight (NLOS), as well as for directional and omnidirectional scenarios, respectively. Comparative results regarding the rms delay spread and the angular spread of the channel were also presented. Similar measurements and results at 142 GHz in different outdoor locations were also presented in [7] and [9]. Moreover, in [7] the spatial consistency of the channel was also assessed. Rooftop surrogate satellite measurements in outdoor locations at 142 GHz were initially reported in [9], where the foliage blockage for the LOS path was examined. These were further analyzed in [10], where the interference between satellite and terrestrial links was examined in conjunction with the elevation angle. The measurement parameters obtained in [6] and [7] were exploited for coverage analyses in [11], providing simulations for spectral efficiencies. Furthermore, path loss results based on measurements in outdoor locations between 138 and 163.2 GHz were provided in [12], where the validity of the fixed intercept (FI) and CI path models was examined. Angular spread profile results for LOS and NLOS outdoor locations (120–165 GHz) were presented in [13], where directional and omnidirectional antenna configurations were examined and it was found that FI model predicts accurately the measured path loss.

In this context, it is really compelling to characterize the wireless channel above 100 GHz and develop models, especially in outdoor urban locations, where directional short-range links will primarily be established in order to compensate the increased path loss. Therefore, it is essential to conduct a rigorous study of the D-band channel and deliver, apart form path loss results, all the related propagation parameters that describe its frequency selective characteristics. The aforementioned research results aimed at characterizing the directional features of the channel, delivering relative path loss and power angular spectrum parameters. Few papers exist, for similar outdoor locations, which provide detailed frequency selective parameters of the channel [5], [6], [7], [8].

This paper introduces a comprehensive propagation study that relies on extensive ray-tracing simulations, launched at 140 GHz, taking into consideration an urban environment. The scenarios involve above and below rooftop propagation, as well as LOS and NLOS conditions. Three different antenna configurations are also considered. In addition to path loss statistics, relative features that determine the frequency selectivity and the fading severity of the channel are obtained and modeled. The propagation study is focused on assessing and modeling the temporal (time-delay) characteristics of the wideband channel, based on different scenarios. All the produced parameters are compared and evaluated with existing measured values for similar outdoor scenarios found in the literature. Preliminary results only for LOS locations and below rooftop propagation can be found in [14]. Related simulations and channel modeling using a multi-ray model, although for an indoor scenario, were presented in [15]. There, the simulated results were validated with measured parameters found in the existing literature at 0.06, 0.3, and 1 THz. Finally, in [16], software-based ray-tracing simulations were conducted in outdoor urban locations at 150 GHz. However, the provided results are not validated with existing measurements. The major contributions of this work are summarized below:

- path loss and shadow fading results are presented and modeled, for LOS and NLOS propagation conditions and different antenna scenarios,
- representative power delay profiles (PDPs) are obtained for the corresponding scenarios from which all the statistical properties of the time delay, coherence bandwidth, signal-to-self-interference ratio, and delay window parameters are delivered, whereas models are provided that describe the relation between them,
- the channel parameters that are produced from the simulations are validated with existing experimental measurements at D-band for similar outdoor locations,
- a multi-cluster PDP model is proposed, resolving the relative attributes that describe the clusters' and the rays' intra- and inter-arrival characteristics, as well as their decaying behavior.

The rest of the paper is organized as follows. The detailed simulation environments and methods are outlined in Section II. The path loss analysis and modeling as well as the atmospheric effects are evaluated and presented in Section III. The data processing, the derivation, and the statistical analysis of the relative wideband channel characteristics are comprehensively described in Section IV. Finally, the modeling of the PDPs, along with their relative attributes, is provided in Section V, followed by interesting conclusions in Section VI.

II. SIMULATION ENVIRONMENT AND PROCEDURE

The deterministic simulation was commenced using Advanced Topographic Development & Images, "ICS Telecom" [17], a commercial tool able to produce different propagation analyses up to 300 GHz, employing ray-tracing methods using three-dimensional (3D) digital maps. The high-resolution digital terrain map (DTM) represents an urban area, downtown Athens, Greece. It has a resolution

TABLE 1. Simulated scenarios and antenna characteristics.

Scenario	Locations		Tx	Rx	G_{Tx}	G_{Rx}	h_{Tx}	h_{Rx}
	LOS	NLOS			[dBi]	[dBi]	[m]	[m]
1	8	7	D	D	18	18	32	1.7
2	8	7	D	D	21	21	5	1.7
3	5	4	O	D	2	18	5	1.7

O: omnidirectional antenna, D: directional antenna.

of 0.4 m, embodying all the buildings' walls, roofs, and superstructures, also containing the terrain elevation and buildings' heights. The simulated area is approximately 5 km^2, in the city center of Athens. There exist narrow streets (about 8–10 m wide) that form propagation canyons, central avenues (about 32 m wide), and open squares. The buildings comprise six to nine storeys having an average height between 18 and 28 m.

The three different areas of Athens' city center with the examined propagation scenarios are depicted in Fig. 1. The green stars indicate each transmitter (Tx) location, whereas the green and red triangles represent the receiver (Rx) positions for LOS, and NLOS conditions, respectively. Scenario 1 represents above-rooftop propagation with an open square and surrounding narrow streets. The Tx is placed at a height of 32 m above the ground (assuming a mast of 4 m and the building height is 28 m). The Rx is fixed at 1.7 m above the ground. Both Tx and Rx antennas have a gain of 18 dBi and half-power beamwidths (HPBWs) of 24° in azimuth and elevation planes, respectively. On the whole, 15 directional links are studied that incorporate 8 LOS and 7 NLOS locations for distances between 53 and 447 m. Scenarios 2 and 3 involve below-rooftop propagation where the Tx is placed at a height of 5 m above the ground (e.g., mounted on lampposts), and the Rx is fixed at 1.7 m above the ground. Scenario 2 examines a typical street canyon with narrow crossroads. Narrow-beam antennas are considered for both Tx and Rx, having a gain of 21 dBi and HPBWs of 16.5° in azimuth and elevation planes, respectively. Fifteen locations are examined, including 8 LOS and 7 NLOS directional links for distances in the range of 41–294 m. Scenario 3 considers a large square surrounded by narrow and wide streets. The Tx and Rx heights are similar with Scenario 2. The Tx incorporates a 2.2–dBi omnidirectional antenna with a HPBW of 78° in the elevation plane, whereas the Rx antenna has a gain of 18 dBi with HPBWs of 24° in azimuth and elevation planes, respectively. There are 9 studied locations with 5 LOS and 4 NLOS links, for distances between 68 and 213 m. Table 1, presents in brief the simulated scenarios and the antenna characteristics. In Scenarios 1 and 2 the Tx and Rx antennas are always oriented in 3D space, maximizing the antenna gain in order to compensate the increased path loss, whereas in Scenario 3 only the Rx antenna is oriented to the Tx. Finally, the corresponding Tx output power is selected 10 dBm at the input of each antenna. The transmitted bandwidth is selected 1 GHz (baseband) that results in a time resolution of 1.0 ns.

FIGURE 1. Urban propagation environment in Athens city center. (a) Scenario 1. (b) Scenario 2. (c) Scenario 3. The photos are taken from Google Earth™.

The tool delivers a full 3D deterministic simulation, where the multiple rays are generated from a ray-launching process. Apart from the direct ray, additional propagation mechanisms are taken into account such as reflection, diffraction, and diffuse scattering. The diffraction is calculated according to the

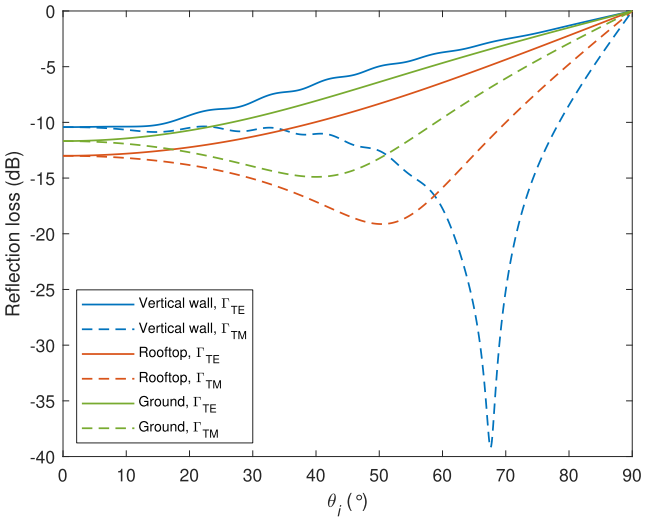

FIGURE 2. Reflection loss versus incidence angle for parallel and perperndicular polarization.

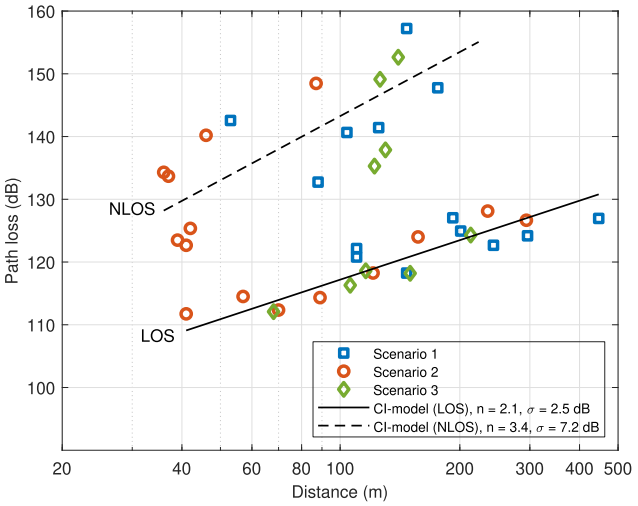

FIGURE 3. Path loss versus distance for LOS and NLOS locations. The CI-model is fitted to the simulated path loss data.

Uniform Theory of Diffraction (UTD) [18]. For the diffuse scattering, the modified Beckmann-Kirchhoff theory [19] is adopted, which provides a good approximation considering large angles of incidence and scattering [15]. The reflection and transmission coefficients are calculated using the boundary model [20], where the rays are refracted and traced inside the materials. The walls of the building blocks are made of double-sided bricks (9 cm) covered with plaster (2 cm) and paint (2 mm) with extruded Polystyrene (5 cm) in between. The rooftops are made of concrete (25 cm) and covered with a strip of insulating asphalt (2 cm) that contains Polyethylene. The refractive indexes and absorption coefficients for those materials are selected from [21] and [22]. For the ground reflections, very dry ground is considered as a material, and the relative refractive and absorption coefficients are taken from [23].

The reflection losses versus incidence angle, θ_i in degrees, for the above-mentioned materials, are shown in Fig. 2, for parallel and perpendicular polarizations. Vertical polarization is selected for the transmitted signal (i.e., perpendicular polarization), therefore, Γ_{TE} is considered for the rays reflected from the vertical walls, and Γ_{TM} for the rays reflected from the ground. Reflections from the rooftops are not encountered in Scenario 1 (roof-to-street propagation) because of the height difference between the terminals. According to Fig. 2, the calculated minimum reflection loss from the walls and the ground, is –10.5 dB, and –15 dB, respectively. The transmission loss is severe at 140 GHz, and all the building constructions virtually block the signal, being non-transparent. For example, the calculated transmission loss for the vertical walls is –115 dB (for $\theta_i = 45°$), and higher than –240 dB for the rooftops. Diffraction loss is also very high at 140 GHz and can exceed 40 dB depending on the diffraction angle [5]. However, as it will be shown in Section IV, diffracted components can be encountered but for shallow diffraction angles (i.e., lower than 5°).

Wideband results can also be obtained resolving the destructive and constructive properties of the propagating waves, which are influenced by the time difference between the direct and the rest of the multipath components (MPCs). The power delay profile can also be extracted [24]. Applying the ray tracing methods, the software resolves all the MPCs in the propagation area and produces an output with the power-delay samples. Finally, the received power at each Rx location is calculated and the minimum Rx threshold is set to –150 dBm.

III. PATH LOSS AND ATMOSPHERIC PHENOMENA

The obtained receiver power samples at each Rx location are used to calculate the path loss. De-embedding the antenna gains, the path loss, in decibels, is given by

$$PL(d) = P_{\mathrm{Tx}} + G_{\mathrm{Tx}} + G_{\mathrm{Rx}} - P_r(d) \tag{1}$$

where P_{Tx} indicates the Tx power in dBm, G_{Tx}, G_{Rx} denote the Tx and Rx gains, respectively (maximized for each link), P_r is the received signal power, in dBm, and d the direct distance between Tx and Rx. It is worth commenting that the maximum gain is removed, because the antennas are oriented during the simulation as mentioned in Section II.

The path loss provides valuable information about the coverage range of the wireless link. Fig. 3 illustrates the simulated path loss versus distance for each examined scenario and propagation condition. It is found in the range of 112–128 dB in LOS links, and increases up to 123–164 dB in NLOS cases, depending on the distance. The excess loss between LOS and NLOS conditions is about 20.2 dB, on average. The additional path loss exhibited in NLOS locations implies that only short range links can be established where the dominant mechanisms are reflection and scattering [25]. This points out the requirement for narrow-beam highly directional antennas in all sub-THz systems. Thus, future wireless links will necessitate fast and rigorous

TABLE 2. Simulated path loss parameters for CI model. The results are compared with existing measured parameters.

Scenario	n		σ [dB]	
	LOS	NLOS	LOS	NLOS
1	2.1	3.4	3.3	7.6
2	2.1	3.5	2.1	6.9
3	2.0	3.2	1.3	7.9
Overall	2.1	3.4	2.5	7.2
Measurements				
[7]:	n = 2.0, σ = 2.9 dB (directional LOS)			
	n = 3.2, σ = 7.2 dB (directional NLOS)			
[6], [9]:	n = 2.1, σ = 2.8 dB (directional LOS)			
	n = 3.1, σ = 8.3 dB (directional NLOS)			
	n = 1.9, σ = 2.7 dB (omnidirectional LOS)			
	n = 2.9, σ = 8.2 dB (omnidirectional NLOS)			
[12]:	n = 2.2, σ = 0.3 dB (directional LOS)			

beamforming techniques to detect, acquire and integrate the dominant component in order to preserve and extend the outdoor NLOS link range at frequencies above 100 GHz [26].

A widely adopted model that is used to forecast path loss is the CI model, which has physical relevance as it is linked to the free space loss at a specific reference distance (usually 1 m is convenient and practical) [27]. The path loss, in decibels, is given by

$$PL^{CI}(d) = PL_{FS}(d_0) + 10n\log_{10}\left(\frac{d}{d_0}\right) + \mathcal{X}_\sigma \qquad (2)$$

where d is the distance in meters between Tx and Rx, d_0 denotes the reference distance (selected 1 m), n indicates the path loss exponent, and $\mathcal{X}_\sigma$ is the shadow fading that is modeled by a zero-mean Gaussian random variable with a given standard deviation, σ, in decibels that represents the large-scale variations. Finally, $PL_{FS}(d_0) = 20\log_{10}(4\pi d_0 f/c)$ is the free space loss at the reference distance d_0 (selected 1 m), where f is the frequency in Hz and c is the speed of light ($3 \cdot 10^8$ m/s). The CI model is fitted to the simulated data using the least squares method in order to find n. The results are presented in Fig. 3. The overall values are resolved from all the simulated locations. In LOS cases the path loss exponent is found equal to 2.1 with $\sigma = 2.5$ dB. The corresponding values for NLOS condition are $n = 3.4$ and $\sigma = 7.2$ dB. Based on the obtained results, it is evident that the CI model can accurately predict path loss for wireless links at 140 GHz, especially for LOS locations. Clearly, NLOS propagation condition demonstrates a higher path loss exponent compared with LOS. This is also evident in Table 2, where the path loss exponent and shadow fading parameters are also presented for each scenario. In LOS links the path loss exponent is close to free space in every examined scenario. The use of directional antennas accounts for this observation, thus establishing a strong direct component between Tx and Rx suppressing the rest of the MPCs. On the other hand, NLOS links exhibit higher n, due to the excess loss introduced by blockage

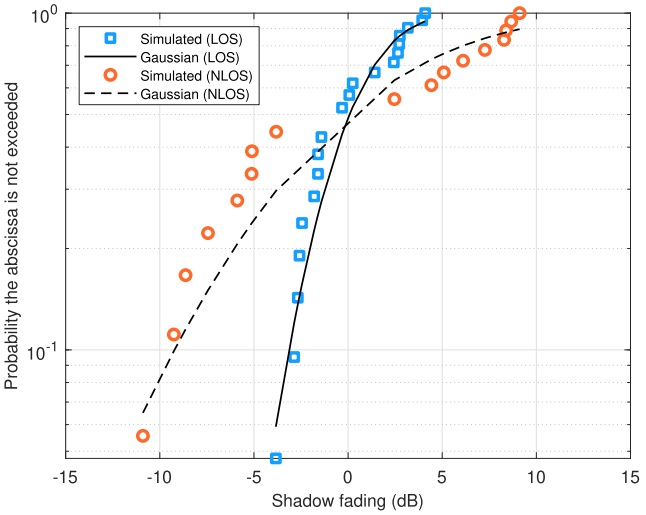

FIGURE 4. Cumulative distribution function of the shadow fading between the simulated data and the theoretical Gaussian distribution for LOS and NLOS conditions.

and mechanisms such as reflections and scattering. Finally, Fig. 4 presents the cumulative distribution function (cdf) of the simulated shadowing fading and the prediction by the Gaussian distribution. As one can observe, the Gaussian distribution approximates very well the obtained shadow fading, confirming the theoretical expectations [27].

Furthermore, the simulated values of n and σ are compared with the values obtained by measurements, found in the existing literature, for similar urban locations. These are summarized in Table 2. The simulated parameters are of the consistent with those reported in [6], [7], [9], and [12]. The path loss exponent for measured LOS links is found close to free space, similar with the simulated values. However, in NLOS links n is found close to 3. The simulated area of Athens incorporates narrow streets compared with New York city, thus creating a dense building environment, accounting for the higher path loss exponents in simulated NLOS locations (3.2–3.5). It is observed that in NLOS cases the measured shadow fading is about 7.2–8.3 dB, also comparable with the simulated results (6.9–7.9 dB) in this work. The simulation tool considers a static environment, another reason accounting for the observed differences.

Another important issue that needs to be considered above 100 GHz, is the effect of the atmospheric phenomena that induce excess loss. These include the oxygen and water vapor attenuation, as well as the attenuation in the case of a rain event. Fig. 5 presents the specific attenuation versus frequency, due to the atmosphere and rain. The specific attenuation for the standard atmosphere combines both oxygen and water vapor absorption, and remains below 2 dB/km, as one can observe in Fig. 5. The specific atmospheric absorption is calculated according to [28] considering a standard atmosphere at sea level [10]. Therefore, for short-range links up to 0.5 km the excess

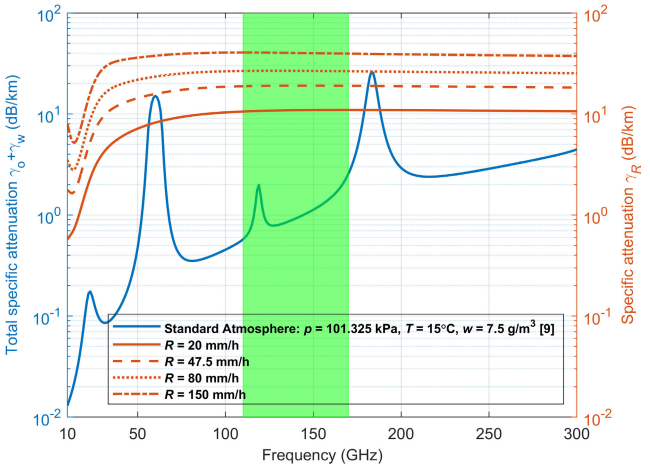

FIGURE 5. Atmosphere and rain specific attenuation as a function of frequency for standard atmospheric conditions and different rain rates. The green area denotes the D-band frequency segment.

loss due to the atmospheric absorption can be disregarded at 140 GHz. Additionally, rain is expected to impose further attenuation in the wireless links. The specific attenuation (in dB/km) is calculated according to [29], considering different rain rates between 20 and 150 mm/h [10], [31]. Vertical polarization is selected. According to Fig. 5, the obtained excess loss is in the range of 10.9–40.2 dB/km. The rainfall rate in Athens region is 47.5 mm/h [30] (i.e., the rainfall rate exceeded for 0.01% of an average year), which entails a specific attenuation of 19.1 dB/km. The maximum distance for a LOS link is 447 m (Scenario 1) that results in an excess loss of 15.6 dB in the case of rainfall. This loss is not restrictive for implementing efficient LOS links at 140 GHz. However, highly directional antennas with accurate beamforming techniques have to be employed. For higher rain rates or greater distances the vitality of such links is expected to be compromised in the event of rain. Path loss incorporating atmospheric absorption and rain attenuation are useful for link budget calculations and can be employed for system-level simulations.

IV. WIDEBAND CHANNEL CHARACTERISTICS

The simulation tool produces an output with power-delay samples that can be used to determine the wideband characteristics of the channel. The PDP can be resolved from the impulse response and is expressed as

$$P(\tau) = |h_b(\tau)|^2 = \sum_k a_k^2(\tau) e^{j\theta_k} \delta(\tau - \tau_k) \tag{3}$$

where a_k^2, τ_k, and θ_k are the power, delay and phase samples, respectively, of the k-th multipath component, $\delta(\cdot)$ stands for the unit impulse function, and $h_b(\tau)$ denotes the baseband impusle response of the channel. Each PDP is normalized to each power gain $P_{norm}(\tau) = P(\tau)/G$ (i.e., the wideband power), where $G = \sum_k a_k^2(\tau)$. A threshold of –30 dB below the maximum component is applied to each profile, below which any component is discarded from further processing [32]. From (3), the mean excess delay, m_τ, the rms delay spread, σ_τ, and the maximum delay $\Delta\tau_{max}$ [33], are calculated according to

$$m_\tau = \sqrt{\frac{\sum_k a_k^2 \tau_k}{\sum_k a_k^2}} \tag{4}$$

$$\sigma_\tau = \sqrt{\frac{\sum_k a_k^2 (\tau_k - m_\tau)^2}{\sum_k a_k^2}} \tag{5}$$

$$\Delta\tau_{max} = \tau_{max} - \tau_{min} \tag{6}$$

In the following the PDPs are provided in terms of excess delay where the first arriving component is shifted so $\tau_{min} = 0$. Therefore, $\Delta\tau_{max} = \tau_{max}$, which indicates the component with the longest delay detected above the imposed threshold. The K-factor that denotes the power of the dominant components to multipath ratio is given by

$$K = 10\log_{10}\left(\frac{a_{max}^2}{a_{mpc}^2}\right) \tag{7}$$

where a_{max}^2 represents the power of dominant component within the PDP and a_{mpc}^2 the power of the remaining MPCs. The dominant component is either the LOS path or the component with the strongest power [34].

Representative PDPs, for selected LOS and NLOS locations are shown in Fig. 6, considering all the examined propagation scenarios. In each plot, the above-mentioned parameters are also indicated. It is evident that the rays arrive in groups of clusters. These are formed from the dominant rays that arrive at the Rx, which include the direct ray, the ground reflected path, the reflections from the building facades and weak diffracted components from the street corners but for diffraction angles lower than 5°. For example in Scenario 1 at LOS location Rx6 (the Tx-Rx distance is 147.2 m), there exist three clusters. Examining Fig. 1(a) and Fig. 6(a), the first cluster contains the direct and the ground reflected ray (along with random scattered components), and the second and third cluster include the reflection from the building facade on the right side of the Rx (as the Rx sees the Tx), and the reflection from the building behind the Rx, respectively (secondary scattered paths are also present). The ground path falls within the first cluster, 2.7 ns after the LOS component (their path difference is about 0.8 m), having a reflection loss of 12.3 dB. The Tx and Rx antennas are oriented as mentioned in Section II. The ground path arrives at the Rx having an angle of 25.1°, which is out of the main beamwidth of the antenna (24°) attenuating about 18 dB. The second reflection in the third cluster has a small reflection loss (2.0 dB) from the building wall but it is further attenuated about 20 dB from the back lobe of the Rx antenna. Similar propagation mechanisms are observed in the same scenario at LOS location Rx10. There, the path difference between the LOS and the ground component is 0.4 m which results in 1.3 ns time difference,

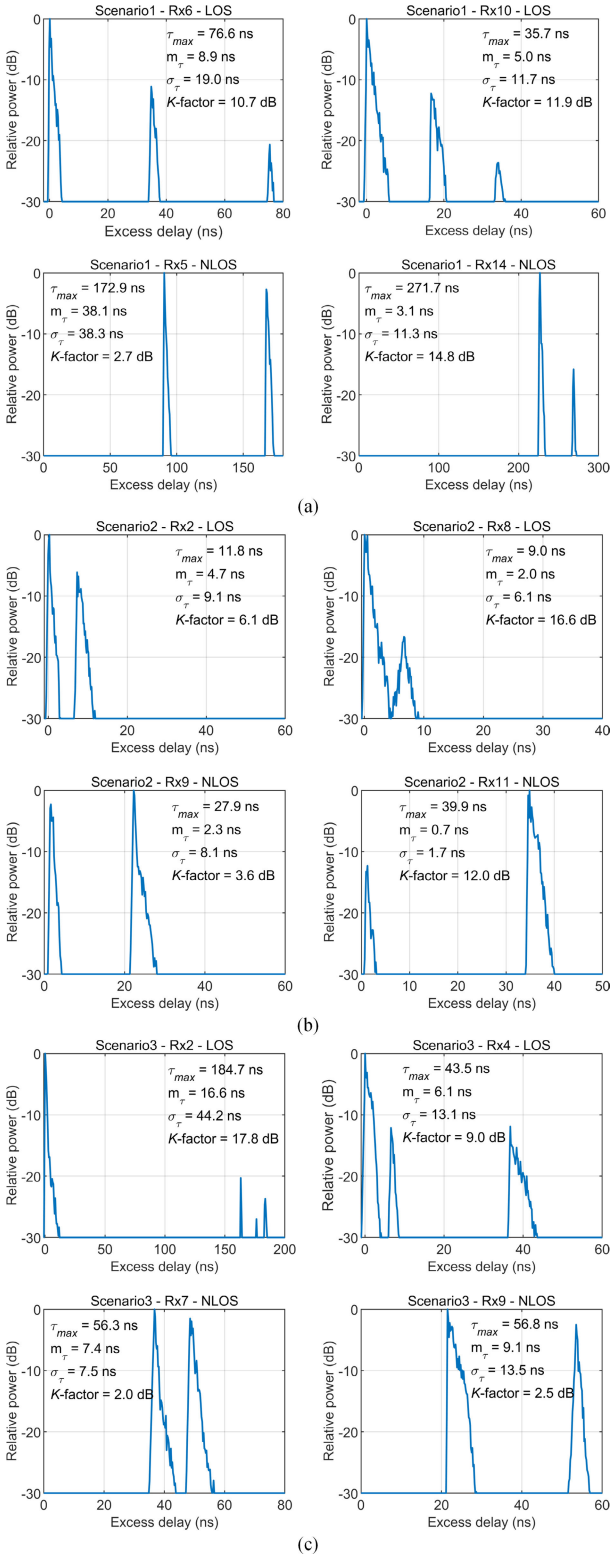

FIGURE 6. Representative power delay profiles for selected LOS and NLOS locations. (a) Scenario 1. (b) Scenario 2. (c) Scenario 3.

still resolvable by the selected bandwidth in the delay domain (1 GHz). Comparable characteristics are also observed in Scenario 3 at LOS location Rx2 (see Fig. 6(c)). The distance of the link is 63 m, having an omnidirectional antenna at the Tx. The three observed clusters that arrive at longer delays (with short inter-cluster delays between them) originate by the reflections from the buildings that surround the Rx (see Fig. 1(c)). Therefore, it can be inferred that multiple clusters are usually formed when the established links are in open spaces (e.g., squares) and the Rx is surrounded by tall buildings. The ground path can still be detected 1.3 ns after the LOS component (their path difference is 0.4 m), having a reflection loss of 12.5 dB. However, for greater distances (e.g., $>$ 65 m) the ground reflection can not be resolved. This stands for the rest of the LOS locations in Scenario 3 and Scenario 2, as well. A wider transmitted bandwidth could be used for this purpose (e.g., 4 GHz) but the limitations imposed by the digital map resolution (0.4 m) would not provide useful results. In any case, all the detected ground reflections in the examined scenarios have negligible impact on the total received power providing paths gains lower than 1 dB.

In NLOS locations one or two main clusters are generally formed as one can observe in Fig. 6. These characteristics are preserved in all of the examined NLOS links, where the dominant propagation mechanism is reflection. For example in Scenario 1 at NLOS location Rx14, inspecting Fig. 1(a) and Fig. 6(a), the first delayed cluster is induced by a single reflection and secondary scattered paths from the building facade behind the Rx. The second delayed cluster originates from a double reflection from the buildings right and behind the Rx (as the Rx sees the Tx). The reflection loss of the double reflected component is about 14.5 dB higher. Similar mechanisms are observed in the same scenario at NLOS location Rx5 but the reflection loss difference is about 4 dB. The direct and the ground reflected paths are totally blocked and do not appear in the PDPs whatsoever. Double- or triple-clustered PDPs are found in LOS conditions but when the Rx is placed in street canyons. See for example the PDPs in Fig. 6(b) for Scenario 2 and LOS locations Rx2 and Rx8 (two clusters) and in Fig. 6(a) for Scenario 1 and LOS locations Rx6 and Rx10 (three clusters). This tendency is observed in every examined scenario when the Rx is placed in streets that form canyons. The narrow streets in conjunction with the directional antennas at the Rx suppress the multipath, allowing specular reflections from the building facades at the right or left of the Rx. The aforementioned findings are reflected in the time delay parameters as well. Therefore, PDPs in NLOS locations result in higher excess delays compared with PDPs at LOS locations, except in cases where long delayed paths are encountered (e.g., in Scenario 3, LOS location Rx2).

Diffracted components are detected but for angles lower than 5°. A representative PDP to describe the specific mechanism is illustrated in Fig. 7, where NLOS location Rx8 in Scenario 3 is selected specifically for this purpose. The first cluster contains the diffracted component from the street corner and secondary paths. In this case, the obstacle height h is 1 m, which results in a diffraction angle $\theta = 2°$. The diffraction loss, L_{diff}, given by the Fresnel integral, is 28.2 dB for $\nu = 5.8$ (dimensionless parameter) [18]. The path gain

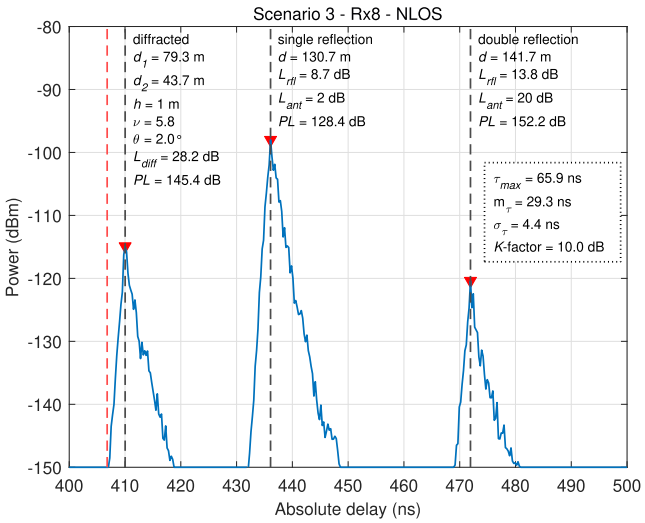

FIGURE 7. Power versus absolute delay for Scenario 3 and NLOS location Rx8. The red dashed vertical line indicates the arrival of the direct path. The Tx-Rx separation is 122 m.

of the diffracted component is 0.5 dB. The second cluster originates from a single reflection from the building at the right side of the Rx (as the Rx sees the Tx), having a reflection loss $L_{rfl} = 8.7$ dB and an excess loss due to the antenna pattern $L_{ant} = 2$ dB (secondary paths from scattered components are also present). Finally, the third cluster is induced by a double reflected path from the building at the right side of the Rx and the building at the back of the Rx. The corresponding reflection and antenna losses are indicated in Fig. 7. Based on the obtained values, the dominant propagation mechanism is reflection, despite the existence of a diffracted path. Similar findings are obtained for NLOS locations Rx9 (see Fig. 6(b)), and Rx14, in Scenario 2. In location Rx9 the diffraction loss is 25.5 dB providing a diffraction gain of 2.1 dB to the received signal power ($h = 0.4$ m, with a diffraction angle of 2.7°). The corresponding values for location Rx14 are $h = 0.4$ m, with an angle of 4.2°. The diffraction loss is 26.8 dB and the provided gain is 1.3 dB. Therefore, in NLOS locations the diffraction mechanism can be encountered but for shallow angles ($< 5°$), providing gains up to 2.1 dB at most. In any other case (i.e., greater angles) the diffracted path is found extremely attenuated and the basic propagation mechanism that dominates the PDPs is reflection. The observed results are congruent with those reported in [5].

Another observation is that when two or more clusters are formed, σ_τ is higher than m_τ. The existence of the clusters in the late time that contain weak reflected components, which strongly affect σ_τ, account for this remark. Only in three NLOS locations (with two and three clusters) m_τ is close or higher than σ_τ, for example Rx5 in Scenario 1, and Rx7, Rx8 in Scenario 3. In this case, these profiles are dominated by strong reflected components that arrive relatively close, which heavily control m_τ, thus increasing its value. Seven PDPs in NLOS locations contain only one

TABLE 3. Statistical properties of the simulated wideband channel properties at 140 GHz. The results are compared with existing measured parameters.

		τ_{max} [ns]	m_τ [ns]	σ_τ [ns]	K [dB]	B_c [MHz]	$W_\tau^{(q)}$ [ns]
Scenario 1	min	29.4	3.1	7.0	2.7	8.9	27.3
	max	271.7	38.1	38.3	14.8	68.4	265.3
	μ	71.5	8.7	15.6	9.0	35.3	72.1
	σ	66.3	8.0	8.0	3.7	17.7	66.1
Scenario 2	min	9.0	0.7	1.7	3.6	32.9	8.2
	max	62.4	8.5	13.2	16.6	161.7	57.6
	μ	24.8	2.5	3.0	11.6	72.7	23.6
	σ	14.6	2.2	2.2	3.5	37.8	14.3
Scenario 3	min	40.2	3.2	4.4	2.0	12.8	38.6
	max	184.7	29.3	44.2	17.8	100.2	183.0
	μ	85.7	11.6	16.5	9.2	42.4	84.1
	σ	55.1	7.9	13.3	5.0	29.9	55.1
LOS	min	9.0	2.0	4.8	6.1	12.8	8.2
	max	184.7	16.6	44.2	17.8	100.2	183.0
	μ	47.6	6.7	14.1	11.9	46.8	46.3
	σ	40.1	3.7	8.7	2.8	22.5	40.9
NLOS	min	27.9	0.7	1.7	2.0	8.9	27.0
	max	271.7	38.1	38.3	14.8	161.7	271.0
	μ	67.6	8.5	11.4	7.4	38.1	66.1
	σ	58.9	9.6	8.8	3.6	41.7	58.9

Measurements	
[5]:	$\mu\{\sigma_\tau\} = 2.8$ ns (directional LOS)
	$\mu\{\sigma_\tau\} = 2.1$ ns (directional NLOS)
	$\mu\{\sigma_\tau\} = 17.0$ ns (omnidirectional LOS)
	$\mu\{\sigma_\tau\} = 20.0$ ns (omnidirectional NLOS)
[6]:	$\mu\{\sigma_\tau\} = 1.7$ ns (directional LOS)
	$\mu\{\sigma_\tau\} = 4.5$ ns (directional NLOS)
[7]:	$\mu\{\sigma_\tau\} = 5.7$ ns (omnidirectional LOS)
	$\mu\{\sigma_\tau\} = 21.9$ ns (omnidirectional NLOS)
[8]:	$\mu\{\sigma_\tau\} = 3.4$ ns (directional LOS)
	$\mu\{\sigma_\tau\} = 1.9$ ns (directional NLOS)
[9]:	$\tau_{max} = 132$ ns (simulated omnidirectional LOS)

μ: numerical mean, σ: numerical standard deviation.

cluster, getting on average $m_\tau > \sigma_\tau$. In this case, there are many MPCs that arrive early in time, thus influencing m_τ. It is worth mentioning that the majority of the examined PDPs contain two clusters (22 locations), one PDP is formed by four clusters and 9 locations are found to contain three clusters. The relation between those delay parameters can be described by the spreading factor that is defined as $s_f = m_\tau/\sigma_\tau$, which provides a measure of the dispersion of the signal in a wideband system [35]. If $s_f > 1$, then the majority of the MPCs arrive early in time, producing high power concentration in the first arrived cluster, whereas if $s_f < 1$, there is an indication that the MPCs arrive at the middle part of the PDP with longer delays, which directly influence σ_τ. The spreading factor is a useful parameter that indicates the distribution of the MPCs within the PDP.

The statistical properties of the corresponding time delay parameters are summarized in Table 3. The results are presented separately for each scenario, as well as for LOS and NLOS conditions. It should be pointed out that the overall statistics are derived from the numerical mean of all the samples. The simulated results are also compared with

parameters obtained by measurements, found in the existing literature (where available), for similar urban locations. These are listed in Table 3. However, only τ_{max}, m_τ, and σ_τ are reported in other measurement campaigns [5], [6], [7], [8], [9]. The rms delay spread is found in the range of 7.0–38.3 ns, 1.7–13.2 ns, and 4.4–44.2 ns, for Scenarios 1, 2, and 3, respectively. Scenario 2 demonstrates the lowest σ_τ, having a mean value of 3.7 ns for LOS and 2.2 ns for NLOS locations, respectively, which is attributed to the street canyon propagation and the narrow-beam directional antennas. These values are comparable with the mean delay spread found in [8], regarding a similar urban street canyon for directional links (3.4 ns and 1.9 ns for LOS and NLOS locations, respectively).

Higher mean values of σ_τ are found in Scenario 1 (15.6 ns) and Scenario 3 (16.5 ns), respectively. The propagation environment in open squares, in which the Rx is surrounded by tall buildings, creates a rich multipath condition that in turn increases the delay spread values. The wider-beam antennas at the Rx (24°) in Scenario 1 and 3, as well as the omnidirectional antenna at the Tx in Scenario 3, account also for the increased delay spread values. In Scenario 3, σ_τ is found 6.5 ns and 25 ns for LOS and NLOS locations, respectively. The specific values are in agreement with the mean delay spread found in [7], despite the fact that the latter were obtained from synthesized omnidirectional PDPs.

Furthermore, LOS locations exhibit higher mean values of σ_τ (14.1 ns), compared with NLOS (11.4 ns). One would expect that NLOS links would suffer from severe multipath resulting in higher delay spread. However, as mentioned previously, the majority of the PDPs in NLOS locations contain one or two clusters (at most), which results in lower delay spread values. The obtained mean σ_τ in this work for NLOS links (11.4 ns), is comparable with the average values taken from [5], [6], and [7], (12.1 ns for directional and omnidirectional NLOS links), for similar microcellular environments. However, in LOS cases the mean delay spread in this work (14.1 ns) is higher than the average values from [5], [6], and [7], (6.8 ns), which is attributed to the wider-beam directional antennas at the Rx, selected in this work. The maximum delay in Scenario 3 is in the range of 40.2–184.7 ns which is consistent with the simulated values found in [9], for similar omnidirectional links.

Fig. 8 presents the cumulative distribution function (cdf) of the mean delay and rms delay spread, respectively. It is evident that both curves are well approximated by the Lognormal distribution, which is consistent with the findings reported in [5] and [36]. The goodness-of-fit is tested employing the Kullback-Leibler divergence criterion [37]. The best fit is achieved minimizing the distance, d_{KL}, between the simulated and the theoretical distribution [38]. Furthermore, the inner plot provides a linear relationship between m_τ and σ_τ for all the locations. The estimated

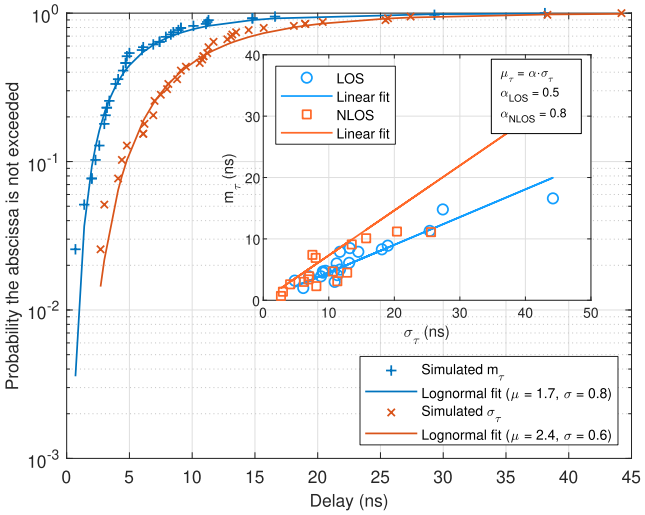

FIGURE 8. Cumulative distribution functions of the mean excess delay and rms delay spread. The inner subplot indicates the spreading factor of those parameters.

function is fitted using the least-squares method. The constant parameter α, shown in Fig. 8, represents the spreading factor. The obtained values are $\alpha_{\mathrm{LOS}} = 0.5$, and $\alpha_{\mathrm{NLOS}} = 0.8$ indicating that $s_f < 1$. In this case, the MPCs with longer delays are distributed in the middle part of the PDPs, which directly affects σ_τ. This is also reflected in the results in Table 3, where the numerical mean of σ_τ is greater than m_τ, in both LOS and NLOS locations.

The K-factor provides the information of how severe is the fading of the channel and a measure of its sparsity (i.e., if the energy of the channel is concentrated on a single or many MPCs) [39]. The simulated values are found to vary between 6.1 and 17.8 dB, and between 2.0 and 14.8 dB in LOS and NLOS locations, respectively. Clearly, in LOS conditions, K-factor demonstrates higher values, implying that the LOS component is the dominant path, which corresponds to a sparser channel. The employed directional antennas account also for this observation. For example, in Scenario 2, where high-gain narrow-beam directional antennas are used in a street canyon, the mean K-factor is higher (11.6 dB) compared with Scenario 1 (9.0 dB) and Scenario 3 (9.2 dB), respectively. On the other hand, in NLOS locations, K-factor is reduced on average, indicating the existence of more MPCs (i.e., less sparse channel). There is a relationship between the rms delay spread and the K-factor of a channel, where the latter tends to decrease as σ_τ increases [40]. This is justified in Fig. 9, in which K-factor is plotted against rms delay spread, separately for LOS and NLOS locations. The results indicate that K-factor decreases linearly as σ_τ increases. The estimated linear functions are fitted using the least-squares method.

Assuming that the channel preserves wide-sense-stationary uncorrelated scattering (WSSUS) characteristics [33], the frequency correlation function (FCF) of the channel is obtained applying a Fourier transform to the normalized

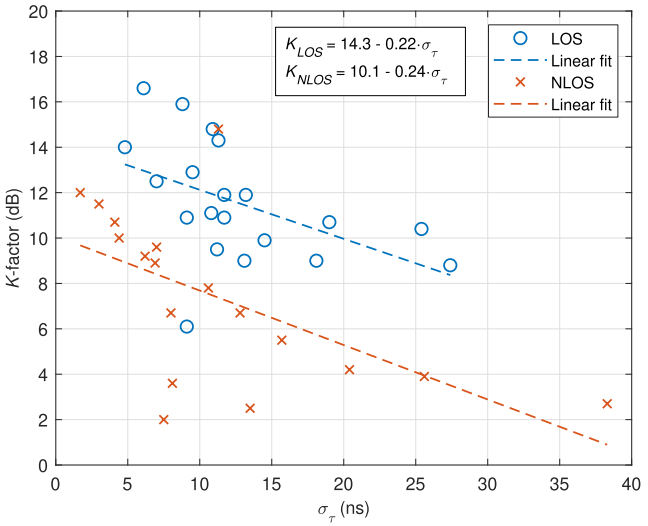

FIGURE 9. *K*-factor as a function of rms delay spread for LOS and NLOS propagation condition.

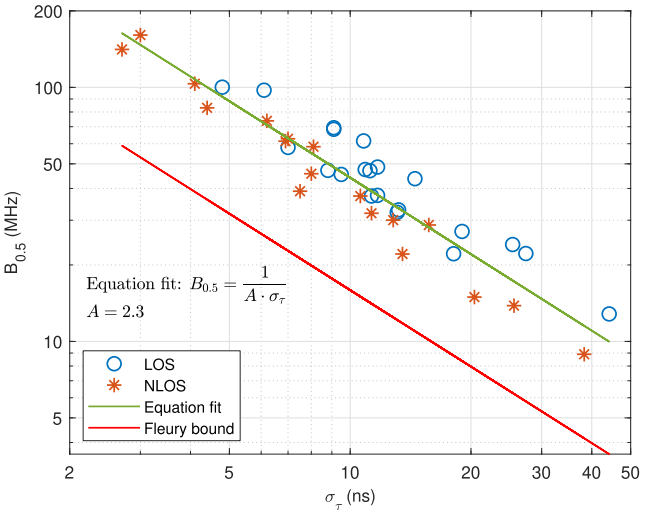

FIGURE 10. Simulated coherence bandwidth versus rms delay spread. The results are plotted in a logarithmic scale.

PDPs according to

$$\tilde{R}_H(\Delta f) = \sum_{k=0}^{N-1} P_{norm}(\tau_k) \exp\left(-j\frac{2\pi k \Delta f \tau_k}{N}\right) \quad (8)$$

where N denotes the number of the MPCs. The FCF conveys a valuable knowledge of the channels' frequency selectivity, accounting for the coherence bandwidth capability, i.e., the maximum available bandwidth that can be exploited at the Rx without introducing harmful inter-symbol interference (ISI). The coherence bandwidth B_c is the minimum number so that $|\tilde{R}_H(B_c)| < k$, where k is the correlation level. In the following, a correlation level of 50% is selected ($k = 0.5$) [41]. The calculated coherence bandwidth is listed in Table 3. Its mean values are found 46.8 and 38.1 MHz for LOS and NLOS conditions, respectively. Overall, the coherence bandwidth varies between 8.9 and 161.7 MHz. A scatter plot of the simulated coherence bandwidth as a function of σ_τ is depicted in Fig. 10, for LOS and NLOS locations. The coherence bandwidth demonstrates an inversely proportional trend against the rms delay spread and using a least-squares fit is found to be modeled according to the expression.

$$B_{0.5} = \frac{1}{A \cdot \sigma_\tau} \quad (9)$$

where $A = 2.3$. The relationship between B_c and σ_τ is an uncertainty function where $B_c \geq 1/(2\pi\sigma_\tau)$ [42], which is the Fleury bound, denoted by the red line indicated in Fig. 10. It is apparent that the coherence bandwidth values are much lower than the selected bandwidth of 1 GHz, thus implying that the small-scale fading characteristics vary substantially over the bandwidth. This can be proved beneficial if frequency diversity is applied, enhancing the efficacy of the channel over small-scale fading events. However, those frequency selective characteristics could be detrimental to digital beamforming coefficients, indicating the necessity for higher overhead feedback, provided that a feedback beamformer is adopted [5].

Two additional parameters that provide insightful information about the channels' characteristics are the signal-to-self interference ratio (SSIR) and the delay window [43]. The former, also known as interference ratio, provides the maximum ratio of the power within a window length $\Delta\tau$, to the power outside of that window. It is calculated according to.

$$Q_\tau^{(\Delta\tau)}(\tau_0) = 10\log_{10}\left[\frac{\sum_{\tau_0-\Delta\tau/2}^{\tau_0+\Delta\tau/2} a_k^2\tau_k}{\sum_k a_k^2\tau_k - \sum_{\tau_0-\Delta\tau/2}^{\tau_0+\Delta\tau/2} a_k^2\tau_k}\right] \quad (10)$$

where τ_0 is the starting time. The SSIR is calculated by searching the proper τ_0 that maximize it. This is a common technique operated by current receiver systems, which they attempt to select the sampling time and synchronization (i.e., the effective window), properly in order to maximize SSIR [42]. The physical rationale of SSIR is that conveys the self-interference of a system where everything that falls outside the considered window is regarded as (statistically almost independent) interference that behaves virtually as noise.

The delay window describes the appropriate length of the minimum time window so that SSIR reaches a certain level equal to q dB. It is defined as [43]

$$W_\tau^{(q)}(\tau_0) = \min_{\tau_0}\{\Delta\tau\}|_{q=Q_\tau^{(\Delta\tau)}(\tau_0)} \quad (11)$$

The SSIR values are directly related to the delay window. In channel characterization studies it is preferable to select the duration of the delay window so that the SSIR is maximized. A representative paradigm is depicted in Fig. 11, where the delay window is plotted versus SSIR for three different locations. For example, in LOS location Rx10 the SSIR is

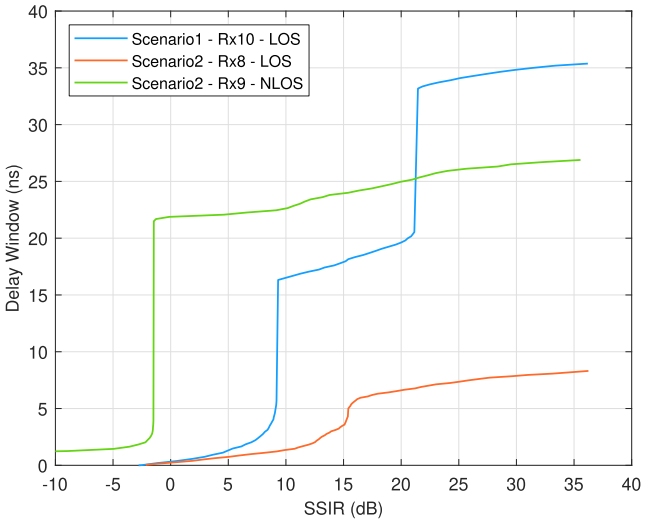

FIGURE 11. Indicative variation plot of the delay window versus SSIR.

maximized for $q = 36.2$ dB, thus getting a delay window of 35.1 ns. It is evident that the delay window increases with increasing SSIR. The statistical properties of the delay window parameter from all the simulated PDPs are listed in Table 3. These values are obtained for the maximum SSIR, where the delay window ranges from 8.2 up to 271.0 ns. The mean delay window is found 46.3 and 66.1 ns for LOS and NLOS locations, respectively, being consistent with the results found in [5].

A general observation is that $W_\tau^{(q)}(\tau_0)$ exhibits slightly lower values compared with τ_{max}. The difference is that the latter parameter depends on the longest detected component which in many cases could be random noise. On the other hand, the calculation of the delay window is based on the power of the received MPCs, attempting to discriminate between useful and harmful signal energy, where long delays are regarded as harmful. System planners select the receivers' effective window length to be longer than the values of the channels' τ_{max} or σ_τ. However, it is more convenient to select the effective window be longer than $W_\tau^{(q)}(\tau_0)$ as this conveys the self-induced quasi co-channel interference induced by delayed MPCs that could be harmful to system receivers [42]. The estimation of this factor is very critical because in orthogonal frequency division multiplexing (OFDM) modulation schemes, the duration of the guard interval T_G (or cyclic prefix) in the frame, should be longer that $W_\tau^{(q)}(\tau_0)$ to prevent ISI at the Rx. Based on the results in Table 3, the cyclic prefix should have a width of tens or even hundreds of ns, which denotes the necessity for up to hundreds of kHz subcarrier spacing in the worst case.

V. POWER DELAY PROFILE MODELING

Based on the multiple clustering form of the obtained PDPs, described in Section IV, where clusters of rays arrive at the Rx at different delays, depending on the number of the reflections and their path lengths, (3) can be written according to

$$P(\tau) = \sum_{l=1}^{L} \sum_{k=1}^{K_l} a_{k,l}^2 e^{j\theta_{k,l}} \delta(\tau - T_l - \tau_{k,l}) \tag{12}$$

where L indicates the number of clusters, K_l stands for the number of the rays within the cluster, $a_{k,l}^2$, $\tau_{k,l}$, and $\theta_{k,l}$ denote the power, delay and phase samples, respectively, of the k-th MPC in cluster l. Finally, T_l designates the delay of arrival of the l-th cluster, and $\tau_{k,l}$ is the delay of the k-th MPC with respect to T_l [44]. The first cluster represents the dominant component (i.e., the LOS path or the component the highest power). Assuming that the peak of each cluster, as well as the power of the incident rays within a cluster, both degrade exponentially on a linear scale, the average power of each k-th component within the l-th cluster is modeled as follows

$$\overline{a_{k,l}^2} = \overline{a_{1,1}^2} e^{-T_l/\Gamma} e^{-\tau_{k,l}/\gamma} \tag{13}$$

where $\overline{a_{1,1}^2}$ denotes the average power of the first arrived component in the first cluster, and Γ, γ denote the power-delay time constant of the clusters and rays, respectively (i.e., the power decay factors) [45]. It should be pointed out that for a single cluster, (12) is converted to (3), and $e^{-T_l/\Gamma} = 1$, in (13). Expressing the modeled PDPs in decibels, (13) can be written as

$$\overline{a_{k,l}^2}\,[\text{dB}] = 20\log_{10}\overline{a_{1,1}} - \left(\frac{T_l}{\Gamma} + \frac{\tau_{k,l}}{\gamma}\right) 10\log_{10}(e) \tag{14}$$

The exponential relationship between the linear power and the excess delay in (13), is converted into a simple linear dependence when the normalized power is regarded in a logarithmic scale in (14). In the following, the clusters were distinguished by finding the first arrived (and strongest) component of each cluster (peak power) and plotted versus excess delay. Then, Γ is determined from (14), by performing a linear regression, having as dependent variable the peak power of each cluster, in decibels, and as independent variables the related delays of those peaks. In this case $\tau_{k,l}$ is considered as zero. Let S be the slope of the fitted line (i.e., the linear line that is fitted to the clusters' peaks), it is converted to the exponential cluster decay constant according to $\Gamma = -10\log_{10}(e)S$, where e is the exponential constant (2.718). In the same way, the intra-cluster decay constant γ, can be estimated by conducting a linear regression to the power of the rays (subpaths), in decibels, as a function of their excess delays. Similarly, if s_l is the slope of the regression line (i.e., the linear line that is fitted to the subapaths' peaks within a cluster), it is converted to the exponential ray decay constant using $\gamma = -10\log_{10}(e)s_l$.

The next step is to model the ray and cluster arrival rates. These are assumed to be approximated by a stochastic Poisson process, therefore, the inter-cluster and inter-ray delays can be expressed by an exponential probability density

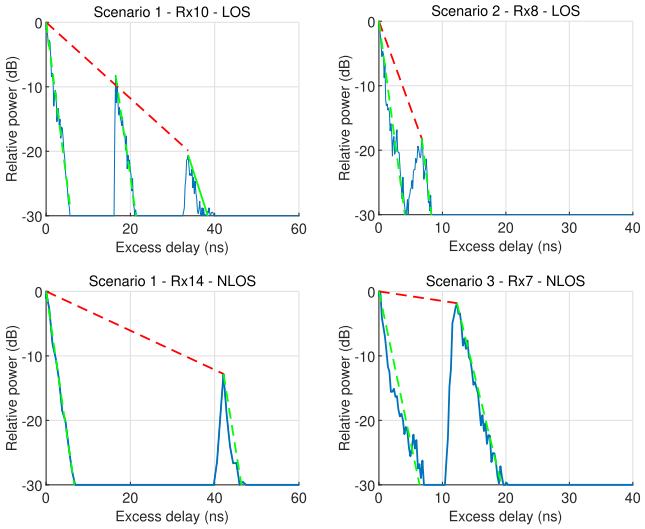

FIGURE 12. Representative power delay profiles and model fitting for selected LOS and NLOS locations. The green dashed line indicates the model fit of the rays within each cluster and the red dashed line denotes the model fit of the clusters.

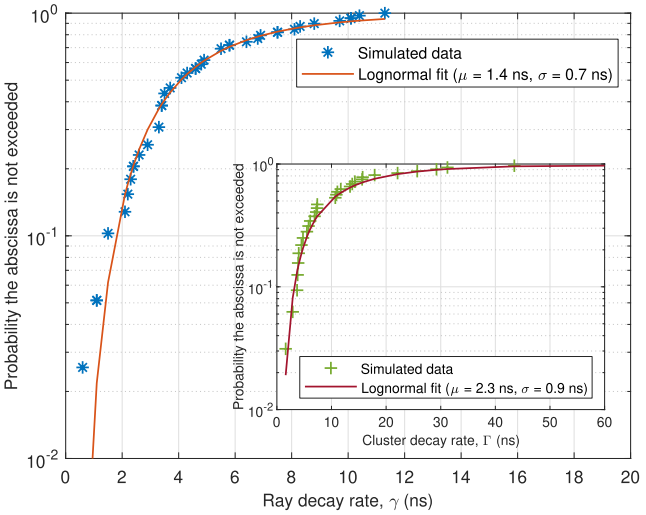

FIGURE 13. Cumulative distribution functions of the ray and cluster decay rates (inner subplot).

function (pdf) according to

$$p(T_l|T_{l-1}) = \Lambda e^{\Lambda(T_l - T_{l-1})} \tag{15}$$

$$p(\tau_{k,l}|\tau_{k-1,l}) = \lambda e^{\lambda(\tau_{k,l} - \tau_{k-1,l})} \tag{16}$$

where Λ and λ, denote the cluster and ray arrival rates, respectively [45]. The parameters of Λ and λ can be estimated by fitting the cdf of the simulated inter-arrival values to the conditional functions given by (15) and (16), respectively. The Kullback-Leibler divergence criterion is also employed as a goodness-of-fit measure. The cluster inter-arrival time is estimated by subtracting the time delay T_l of the l-th cluster from the previous one. The same method is applied for the calculation of the ray inter-arrival time. Apparently, there is no relative arrival delay for the first incoming ray and cluster. In the following, the associate parameters of the multi-cluster model Γ, γ, Λ, and λ, are calculated as described above, and these features actually represent the large-scale fading parameters of the examined propagation channel.

One up to four clusters are clearly distinguished from the obtained simulated PDPs, as also shown in Fig. 6. Accordingly, the model is fitted to the PDPs and indicative results for selected LOS and NLOS locations are presented in Fig. 12. The green dashed lines denote the model fit of the rays within each cluster from which γ is obtained. Accordingly, the regression line for the clusters is denoted with the red dashed lines, thus estimating the cluster decay factor Γ. The coefficient of determination (R^2) [46], associated with each fitted PDP, is found in the range of 0.85–0.95, demonstrating a good agreement between the simulated and the proposed model, as one can observe in Fig. 12. Similar results are realized for the rest of the simulated PDPs. A general observation is that the linear line of the rays exhibit a steeper slope compared with the clusters' inclination, which entails that the ray decay factor is expected to be reduced compared with the cluster decay factor (i.e., the rays within the cluster attenuate faster). This is probably due to the higher attenuation of the random scattered paths in conjunction with the directional antenna patterns at the Rx, thus phasing out the MPCs much faster within the cluster (this is generally observed in every examined scenario). On the other hand, the existence of clusters that arrive at longer delays, compared with the first cluster, results in a lower inclination of the fitted line, producing higher Γ values (especially in Scenarios 1 and 3). This is attributed to the reflected paths in the propagation channel from the buildings' facades, thus establishing longer path lengths. The open spaces and the wider streets in Scenarios 1 and 3, account for this observation, as well.

The cdf of the ray and cluster decay rates are depicted in Fig. 13, where it is obvious that $\Gamma > \gamma$. The results are obtained from all the simulated locations combining LOS and NLOS conditions. Both empirical distributions are well approximated by the Lognormal distribution as it is evident. The corresponding parameters of the Lognormal distribution are found $\mu = 2.3$ ns, $\sigma = 0.9$ ns, and $\mu = 1.4$ ns, $\sigma = 0.7$ ns, for Γ, and γ, respectively. Furthermore, the cdfs of the intra- and inter-cluster delays are presented in Fig. 14. The empirical inter-arrival rates are modeled with the exponential distribution (i.e., Poisson process), delivering, on average, $\lambda^{-1} = 2.83$ ns, and $\Lambda^{-1} = 22.9$ ns for the ray and cluster inter-arrival times, respectively. It is obvious that the clusters exhibit longer arrival delays as it is expected. The empirical cdfs are produced grouping the inter-arrival times from all the simulated locations.

The numerical results of the above-mentioned parameters are summarized in Table 4 for the three examined scenarios, as well as for LOS and NLOS conditions. The mean and standard deviation of each attribute is provided. The results

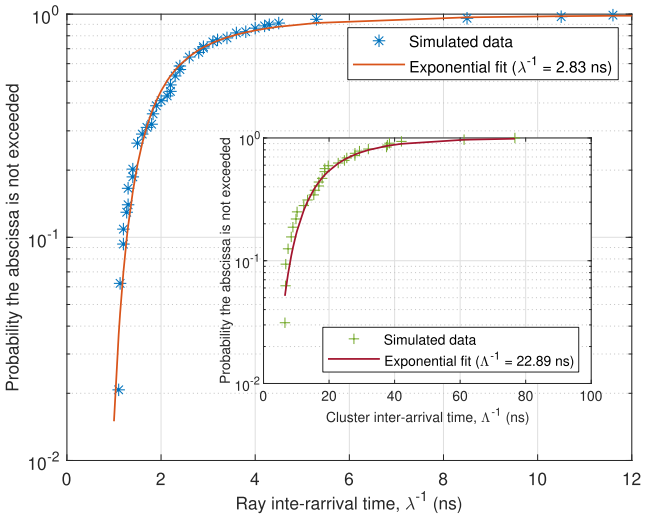

FIGURE 14. Cumulative distribution functions of the ray and cluster inter-arrival rates (inner subplot).

TABLE 4. Statistical properties of the parameters of the multi-cluster model.

		Λ^{-1} [ns]	λ^{-1} [ns]	Γ [ns]	γ [ns]
Scenario 1	μ	32.4	3.1	19.3	6.0
	σ	15.9	1.1	23.6	1.9
Scenario 2	μ	10.1	1.9	4.2	2.5
	σ	3.5	0.4	1.3	0.9
Scenario 3	μ	25.9	2.8	21.1	6.9
	σ	13.8	1.1	11.1	3.0
LOS	μ	20.2	2.2	9.1	4.6
	σ	13.3	0.6	6.2	2.5
NLOS	μ	28.1	3.2	25.1	5.2
	σ	18.3	1.2	25.2	2.9

μ: numerical mean, σ: numerical standard deviation.

justify the previous remarks, where in any case $\Gamma > \gamma$, and $\Lambda^{-1} > \lambda^{-1}$. Another observation is that in Scenario 2 the ray and cluster inter-arrival times are lower compared with Scenario 1 and 3, respectively. The propagation environment accounts for these differences. In Scenario 2, a narrow street canyon channel is involved, and along with the exploitation of narrow-beamwidth directional antennas that suppress multipath, there exist one or two main reflecting surfaces with fast vanishing MPCs (induced by random scattered paths). The closely separated surfaces due to the narrow streets entails a lower cluster arrival rate Λ^{-1} (i.e., the delay between the cluster arrival is reduced). This is also reflected to the power decay factors, as well, where Scenario 2 demonstrates lower values compared with the other two. On the other hand, in Scenarios 1 and 3 the propagation channel involves wider streets and open squares (especially Scenario 3), as well as wider-beam antennas. Thus, there exist additional reflecting surfaces around the Rx, inducing a higher number of clusters with relatively longer delays, increasing all the related parameters of the model. Comparing LOS and NLOS cases, the latter exhibits higher cluster inter-arrival time and decay factor as one can observe in Table 4. However, the numerical mean of λ^{-1} and γ values is comparable, indicating that the MPCs within each cluster arrive and attenuate in a similar way.

VI. CONCLUSION

This paper presented a detailed propagation study based on ray-tracing simulations in an urban environment at D-band. Different propagation scenarios and antenna configurations were examined. The simulated path loss was found to be well approximated by the CI model delivering path loss exponents equal to 2.1 and 3.4 for LOS and NLOS conditions, respectively. The corresponding shadowing factors were found 2.5 and 7.2 dB, respectively. Directional LOS links are feasible for distances up to 0.5 km, but only short range NLOS links can be established (100–150 m), where the dominant propagation mechanism is reflection. Diffracted paths were also encountered but for angles up to 5°, providing path gains up to 2.1 dB. Rainfall events can compromise both LOS and NLOS links, which points out the necessity for narrow-beam highly directional antennas for outdoor systems above 100 GHz. Path loss, including rain attenuation and atmospheric absorption is useful for link budget calculations, providing accurate service-range and outage estimations, as well as rigorous interference results.

Based on the wideband parameters, the simulated channel exhibited frequency selective characteristics. The mean rms delay spread was found in the range of 4.8–44.2 ns and 1.7–38.3 ns, for LOS and NLOS conditions, respectively. Is was also observed that when two or more clusters are formed the rms delay spread tends to increase compared with the mean delay. To prevent ISI at the Rx, the delay window was proposed, indicating that the cyclic prefix in multicarrier modulation should be selected, in the worst case, longer than 270 ns. The simulated PDPs of the channel were fitted using a multi-cluster model. Its corresponding large-scale attributes were all found to be influenced by the propagation environment and the adopted antenna characteristics. Up to four clusters were observed in LOS locations but only single or double clustered PDPs are composed in NLOS positions.

The simulations, the analyses, and the models presented in this work can serve towards gaining a better understanding of the inherent nature of the propagation channel above 100 GHz, and supporting the design and realization of future 6G outdoor wireless communication systems. The model presented in Section V can be used as a basis to extend the channels' characteristics in the spatial domain, carrying out additional simulations, thus assessing the power-angular and the angular-delay profiles and their relative parameters at 140 GHz.

REFERENCES

[1] H. Viswanathan and P. E. Mogensen, "Communications in the 6G era," *IEEE Access*, vol. 8, pp. 57063–57074, 2020.

[2] I. F. Akyildiz, A. Kak, and S. Nie, "6G and beyond: The future of wireless communications systems," *IEEE Access*, vol. 8, pp. 133995–134030, 2020.

[3] E. Calvanese Strinati, S. Barbarossa, J. L. Gonzalez-Jimenez, D. Ktenas, N. Cassiau, L. Maret, and C. Dehos, "6G: The next frontier: From holographic messaging to artificial intelligence using subterahertz and visible light communication," *IEEE Veh. Technol. Mag.*, vol. 14, no. 3, pp. 42–50, Sep. 2019.

[4] T. S. Rappaport, Y. Xing, O. Kanhere, S. Ju, A. Madanayake, S. Mandal, A. Alkhateeb, and G. C. Trichopoulos, "Wireless communications and applications above 100 GHz: Opportunities and challenges for 6G and beyond," *IEEE Access*, vol. 7, pp. 78729–78757, 2019.

[5] J. Gomez-Ponce, N. A. Abbasi, A. E. Willner, C. J. Zhang, and A. F. Molisch, "Directionally resolved measurement and modeling of THz band propagation channels," *IEEE Open J. Antennas Propag.*, vol. 3, pp. 663–686, 2022.

[6] Y. Xing and T. S. Rappaport, "Millimeter wave and terahertz urban microcell propagation measurements and models," *IEEE Commun. Lett.*, vol. 25, no. 12, pp. 3755–3759, Dec. 2021.

[7] S. Ju and T. S. Rappaport, "140 GHz urban microcell propagation measurements for spatial consistency modeling," in *Proc. ICC IEEE Int. Conf. Commun.*, Montreal, QC, Canada, Jun. 2021, pp. 1–6.

[8] N. A. Abbasi, J. Gomez-Ponce, R. Kondaveti, A. Kumar, E. Bhagat, R. N. S. Rao, S. Abu-Surra, G. Xu, C. Zhang, and A. F. Molisch, "Double-directional channel measurements for urban THz microcellular communications in a street canyon," in *Proc. ICC IEEE Int. Conf. Commun.*, Seoul, South Korea, May 2022, pp. 2876–2881.

[9] Y. Xing and T. S. Rappaport, "Propagation measurements and path loss models for sub-THz in urban microcells," in *Proc. ICC IEEE Int. Conf. Commun.*, Montreal, QC, Canada, Jun. 2021, pp. 1–6.

[10] Y. Xing and T. S. Rappaport, "Terahertz wireless communications: Co-sharing for terrestrial and satellite systems above 100 GHz," *IEEE Commun. Lett.*, vol. 25, no. 10, pp. 3156–3160, Oct. 2021.

[11] Y. Xing, O. Kanhere, S. Ju, and T. S. Rappaport, "Sub-terahertz wireless coverage analysis at 142 GHz in urban microcell," in *Proc. ICC IEEE Int. Conf. Commun.*, Seoul, South Korea, May 2022, pp. 3942–3947.

[12] C. Bian, W. Li, M. Wang, X. Wang, Y. Wei, and W. Zhou, "Path loss measurement of outdoor wireless channel in D-band," *Sensors*, vol. 22, no. 24, p. 9734, Dec. 2022.

[13] B. De Beelde, E. Tanghe, D. Plets, and W. Joseph, "Outdoor channel modeling at D-band frequencies for future fixed wireless access applications," *IEEE Wireless Commun. Lett.*, vol. 11, no. 11, pp. 2355–2359, Nov. 2022.

[14] N. Moraitis and K. S. Nikita, "Propagation study in a dense urban environment at the sub-THz band for future wireless communications," in *Proc. 17th Eur. Conf. Antennas Propag. (EuCAP)*, Florence, Italy, Mar. 2023, pp. 1–5.

[15] C. Han, A. O. Bicen, and I. F. Akyildiz, "Multi-ray channel modeling and wideband characterization for wireless communications in the terahertz band," *IEEE Trans. Wireless Commun.*, vol. 14, no. 5, pp. 2402–2412, May 2015.

[16] M. Z. Aslam and Y. Corre, "Simulated propagation properties for future outdoor sub-THz networks," in *Proc. IEEE 31st Annu. Int. Symp. Pers., Indoor Mobile Radio Commun.*, London, U.K., Aug. 2020, pp. 1–6.

[17] Advanced Topographic Development & Images. *ICS Telecom—Comprehensive Network Engineering on V/U/SHF Bands*. Accessed: Aug. 27, 2023. [Online]. Available: http://www.atdi.com

[18] R. G. Kouyoumjian and P. H. Pathak, "A uniform geometrical theory of diffraction for an edge in a perfectly conducting surface," *Proc. IEEE*, vol. 62, no. 11, pp. 1448–1461, Nov. 1974.

[19] H. Ragheb and E. R. Hancock, "The modified Beckmann–Kirchhoff scattering theory for rough surface analysis," *Pattern Recognit.*, vol. 40, no. 7, pp. 2004–2020, Jul. 2007.

[20] C. A. Balanis, *Advanced Engineering Electromagnetics*. 2nd ed. Hoboken, NJ, USA: Wiley, 2012.

[21] R. Piesiewicz, C. Jansen, S. Wietzke, D. Mittleman, M. Koch, and T. Kürner, "Properties of building and plastic materials in the THz range," *Int. J. Infr. Millim. Waves*, vol. 28, no. 5, pp. 363–371, Mar. 2007.

[22] Z. Chen and J.-C. Cao, "Channel characterization at 120 GHz for future indoor communication systems," *Chin. Phys. B*, vol. 22, no. 5, May 2013, Art. no. 059201.

[23] *Electrical Characteristics of the Surface of the Earth*, document ITU-R P.527-6, International Telecommunication Union, Geneva, Switzerland, Sep. 2021.

[24] T. Garand, "Multipath in ICS telecom," ATDI, Washington, DC, USA, White Paper, Jan. 2005.

[25] N. A. Abbasi, J. L. Gomez, R. Kondaveti, S. M. Shaikbepari, S. Rao, S. Abu-Surra, G. Xu, J. Zhang, and A. F. Molisch, "THz band channel measurements and statistical modeling for urban D2D environments," *IEEE Trans. Wireless Commun.*, vol. 22, no. 3, pp. 1466–1479, Mar. 2023.

[26] S. Sun, G. R. MacCartney, M. K. Samimi, S. Nie, and T. S. Rappaport, "Millimeter wave multi-beam antenna combining for 5G cellular link improvement in New York city," in *Proc. IEEE Int. Conf. Commun. (ICC)*, Sydney, NSW, Australia, Jun. 2014, pp. 5468–5473.

[27] T. S. Rappaport, *Wireless Communications: Principles and Practice*, 2nd ed. Upper Saddle River, NJ, USA: Prentice-Hall, 2002.

[28] *Attenuation by Atmospheric Gases and Related Effects*, document ITU-R P.676-13, International Telecommunication Union, Geneva, Switzerland, Aug. 2022.

[29] *Specific Attenuation Model for Rain for use in Prediction Methods*, document ITU-R P.838-3, International Telecommunication Union, Geneva, Switzerland, Mar. 2005.

[30] *Characteristics of Precipitation for Propagation Modelling*, document ITU-R P.837-7, International Telecommunication Union, Geneva, Switzerland, Jun. 2017.

[31] Z. Qingling and J. Li, "Rain attenuation in millimeter wave ranges," in *Proc. 7th Int. Symp. Antennas, Propag. EM Theory*, Guilin, China, Oct. 2006, pp. 1–4.

[32] R. Schulpen, U. Johannsen, A. B. Smolders, and L. A. Bronckers, "Ambiguity in RMS delay spread of millimeter-wave channel measurements," in *Proc. 17th Eur. Conf. Antennas Propag. (EuCAP)*, Florence, Italy, Mar. 2023, pp. 1–5.

[33] J. D. Parsons, *The Mobile Radio Propagation Channel*. 2nd ed. West Sussex, U.K.: Wiley, 2000.

[34] H. Mi, B. Ai, R. He, X. Zhou, Z. Ma, M. Yang, Z. Zhong, and N. Wang, "Multi-scenario millimeter wave wireless channel measurements and sparsity analysis," *China Commun.*, vol. 19, no. 11, pp. 16–31, Nov. 2022.

[35] A. M. Al-Samman, T. A. Rahman, M. H. Azmi, M. N. Hindia, I. Khan, and E. Hanafi, "Statistical modelling and characterization of experimental mm-wave indoor channels for future 5G wireless communication networks," *PLoS ONE*, vol. 11, no. 9, Sep. 2016, Art. no. e0163034.

[36] L. J. Greenstein, V. Erceg, Y. S. Yeh, and M. V. Clark, "A new path-gain/delay-spread propagation model for digital cellular channels," *IEEE Trans. Veh. Technol.*, vol. 46, no. 2, pp. 477–485, May 1997.

[37] S. Kullback and R. A. Leibler, "On information and sufficiency," *Ann. Math. Statist.*, vol. 22, no. 1, pp. 79–86, 1951.

[38] I. Sen and D. W. Matolak, "Vehicle–vehicle channel models for the 5-GHz band," *IEEE Trans. Intell. Transp. Syst.*, vol. 9, no. 2, pp. 235–245, Jun. 2008.

[39] H. Zhang, R. He, B. Ai, S. Cui, and H. Zhang, "Measuring sparsity of wireless channels," *IEEE Trans. Cognit. Commun. Netw.*, vol. 7, no. 1, pp. 133–144, Mar. 2021.

[40] P. F. M. Smulders, "Statistical characterization of 60-GHz indoor radio channels," *IEEE Trans. Antennas Propag.*, vol. 57, no. 10, pp. 2820–2829, Oct. 2009.

[41] W. C. Jakes, *Microwave Mobile Communications*. Piscataway, NJ, USA: IEEE Press, 1974.

[42] A. F. Molisch, *Wireless Communications*. 2nd ed. West Sussex, U.K.: Wiley, 2011.

[43] A. F. Molisch and M. Steinbauer, "Condensed parameters for characterizing wideband mobile radio channels," *Int. J. Wireless Inf. Netw.*, vol. 6, no. 3, pp. 133–154, Jul. 1999.

[44] A. A. M. Saleh and R. Valenzuela, "A statistical model for indoor multipath propagation," *IEEE J. Sel. Areas Commun.*, vol. SAC-5, no. 2, pp. 128–137, Feb. 1987.

[45] Q. H. Spencer, B. D. Jeffs, M. A. Jensen, and A. L. Swindlehurst, "Modeling the statistical time and angle of arrival characteristics of an indoor multipath channel," *IEEE J. Sel. Areas Commun.*, vol. 18, no. 3, pp. 347–360, Mar. 2000.

[46] G. Gougeon, Y. Corre, and M. Z. Aslam, "Ray-based deterministic channel modelling for sub-THz band," in *Proc. IEEE 30th Int. Symp. Pers., Indoor Mobile Radio Commun. (PIMRC Workshops)*, Istanbul, Turkey, Sep. 2019, pp. 1–6.

NEKTARIOS MORAITIS (Senior Member, IEEE) received the Diploma and Ph.D. degrees in electrical and computer engineering from the National Technical University of Athens, Greece, in 1998 and 2005, respectively.

In 1997, he joined the Mobile Radiocommunications Laboratory, National Technical University of Athens. In 2007, he became a permanent staff as a Laboratory Engineer with the Mobile Radiocommunications Laboratory, National Technical University of Athens. In 2014, he became a Teaching and Research Associate (Faculty Staff) with the School of Electrical and Computer Engineering, National Technical University of Athens. He has more than 90 publications in international journals, conference proceedings, and book chapters. He has involved in many research projects, including channel measurements, modeling, and characterization for wireless communication systems, microwave systems design, and mobile satellite communication systems. He has also participated in European projects, such as ERMIS, SatNEx I and II, and COST 273, 259, 2100, and IC0802 activities. His current research interests include millimeter wave propagation for next generation wireless communications systems, channel measurements, characterization, simulation and modeling for fixed and mobile communications systems, MIMO technology for mobile satellite systems, and biological effects of electromagnetic radiation.

Dr. Moraitis ranked in top 200 reviewers of IEEE TRANSACTIONS ON ANTENNAS AND PROPAGATION (May 2021-April 2022). He has been serving as the Chair for the IEEE Vehicular Technology/Aerospace and Electronic Systems Joint Chapter, Greek Section, since 2020.

KONSTANTINA S. NIKITA (Fellow, IEEE) received the Diploma degree in electrical engineering from the National Technical University of Athens (NTUA), the M.D. degree from the Medical School, University of Athens, and the Ph.D. degree from NTUA.

She is currently a Full Professor with NTUA; a Irene McCulloch Distinguished Adjunct Professor of biomedical engineering and medicine with the Keck School of Medicine and the Viterbi School of Engineering, University of Southern California; and the 2022/2023 Global Chair of the University of Bath. She is the Director of the Mobile Radiocommunications Laboratory. She is also the Founder and the Director of the Biomedical Simulations and Imaging Laboratory, NTUA. Her published work consists of 12 books, more than 200 articles in refereed international journals, 48 chapters in books, over 400 papers in international conference proceedings, and three patents. She has been the technical manager of numerous European and national research development projects. Her current research interests include mobile health, computational bioelectromagnetics, biomedical signal and image processing and analysis, simulation of physiological and biological systems, and biomedical data science. She is a fellow of the American Institute of Medical and Biological Engineering (AIMBE) and the European Association of Medical and Biological Engineering and Science (EAMBES). She has received various honors/awards, one of them, from the Bodossakis Foundation Academic Prize. She served as the Chair for the LS7 Consolidator Grant Panel of the European Research Council (ERC), for granting investigator-driven frontier research in the domain of life sciences. She is the Editor-in-Chief of IEEE TRANSACTIONS ON ANTENNAS AND PROPAGATION and the Founding Editor-in-Chief of the IEEE JOURNAL OF ANTENNAS AND PROPAGATION.